IEEE Access
Multidisciplinary | Rapid Review | Open Access Journal

Received 14 February 2023, accepted 14 April 2023, date of publication 18 April 2023, date of current version 24 April 2023.

Digital Object Identifier 10.1109/ACCESS.2023.3268103

RESEARCH ARTICLE

Speed Response Improvement Design of Electric Motor for Vehicle Electrification Based on Electro-Mechanical Analytic Model

DONG-MIN KIM[1], (Member, IEEE), AND MYUNG-SEOP LIM[2], (Member, IEEE)
[1]Department of Automotive Engineering, Honam University, Gwangju 62399, Republic of Korea
[2]Department of Automotive Engineering, Hanyang University, Seoul 04763, Republic of Korea

Corresponding author: Myung-Seop Lim (myungseop@hanyang.ac.kr)

This work was supported by research fund from Honam University, in 2021.

ABSTRACT According to vehicle electrification trends, the application of electric motors more often occurs. Therefore, in the aspect of the supply instability preparation for rare-earth materials, research on the rare-earth-free motor is getting more attention. Moreover, the electric motor for the vehicles should have not only high power density but also fast response. Especially, electric motors for advanced driver assistant systems or autonomous driving vehicles should have a fast response speed to secure the driver's safety. This paper introduces the electro-mechanical response improvement design of concentrated flux synchronous motors for vehicle electrification. Improvement design is carried out targeting motors for electric power steering system. The development of the electro-mechanical analytic (EMA) model of the electric motor is firstly explained. Then, based on the developed EMA model, electro-mechanical response modeling is performed. Finally, the speed response improvement design is conducted using the developed EMA model. In addition, the results are validated not only in finite element analysis but also experimentally.

INDEX TERMS Concentrated flux synchronous motor (CFSM), electric power steering (EPS), rare-earth free motor, rise time, settling time, speed response.

I. INTRODUCTION

Within the era of vehicle electrification, the demand for electric motors gets increasing. Therefore, the market for electric motors has been enlarged. Consequently, cost competence seized one of the main qualifications for electric motors. However, to secure the cost competency of Neodymium used motor, which is the mainstream, management of rare-earth material is a critical matter. Beyond the automotive area, the vulnerability of rare-earth materials supply chain is a significant topic. The importance of rare-earth elements can also be understood through the studies that have been conducted on the hypothetical impact of supply disruptions on the rare-earth element market [1], [2]. Moreover, there is also the investigation of the environmental effect on rare-earth materials [3].

The associate editor coordinating the review of this manuscript and approving it for publication was Qinfen Lu.

Especially, electric vehicles (EVs) or electrified vehicles are affected a lot by rare-earth materials supply. This is because rare-earth materials are essential for two main components, batteries, and electric motors [4]. Besides, the electric motor is a part used in not only EVs but also hybrid electric vehicles (HEVs) and internal combustion engine vehicles. Therefore, the rare-earth material alternative electric motor is important in the automotive market [5]. For the purpose of the research on excluding technology of rare-earth materials, there are many studies on rare-earth-free motors [6], [7], [8], [9].

Among the rare-earth free motor types, the ferrite magnet used motor has been widely used [10]. Compare to rare-earth-magnet such as Neodymium magnet, ferrite magnet has lower performance. However, the ferrite magnet has a high Curie temperature and positive temperature coefficient of intrinsic coercivity. Therefore, the ferrite magnet is robust at higher temperatures. Moreover, price competitiveness is

good and there is no supply vulnerability of materials for manufacturing [11].

To supplement the comparatively lower performance of ferrite magnets, ferrite magnet motors usually adopt the concentrated flux synchronous motor (CFSM) type. Due to CFSM having the spoke structure, it could have a large amount of permanent magnet usage. Therefore, the power density of CFSM could be similar to the rare-earth magnet motor [12]. Accordingly, researches on CFSM are conducted on various topics. Lee et al. studied CFSM considering the magnetization process of the ferrite magnet [13], and Park et al. dealt with the vibration characteristics of the CFSM [14]. Furthermore, Seok et al. tried to design the hybrid CFSM with rare-earth magnet assist [15].

Furthermore, for automotive applications, safety is paramount. As a result, numerous studies on electric motors for vehicles concentrated on fault tolerance and rapid response. To improve fault tolerance, sensor-less controllability [16], [17] and multiplex winding applications [18], [19] are intensively studied. Otherwise, both design and control approaches are being investigated in order to increase response speed [20], [21].

For a long time, numerous research on the design of electric motors has been conducted using an analytical technique. Recently, Gao et al. studied the analytic model to estimate the torque precisely, by reflecting nonlinearity [22]. Dianati et al. developed the analytic model of the axial flux induction motor, which needs 3-dimensional analysis [23]. And Liang et al. investigated the analytic model of CFSM focusing on tooth saturation [24]. All the above researches have great contributions to estimating the electromagnetic phenomenon. However, they could not consider the mechanical properties.

In this study, the electro-mechanical analytic (EMA) model was proposed. This EMA model could calculate the electrical parameter as well as the mechanical parameter quickly. Therefore, using the suggested EMA model, the design direction was established considering both electrical and mechanical characteristics. According to the determined design direction, the speed response improvement design was performed. Then, the improved model was fabricated and tested. In brief, the contribution of this paper can be highlighted as follows.

- Electro-mechanical analytic (EMA) model of the rare-earth-free motor was suggested.
- Speed response improvement design was performed maintaining electrical performance.
- Not only speed response, but also the electrical performance of the improved model was experimentally validated.

The organization of this paper is followed. First, Section II introduces the analytical modeling of electro-mechanical parameters for CFSM, such as back electromotive force (back EMF), inductance, winding resistance, and moment of inertia. Section III then introduces speed response modeling, which is based on the developed EMA model. Finally, in Section IV, the developed EMA model is validated by comparing the parameter calculation results from finite element analysis (FEA). Subsequently, the result of the speed response improvement design is explained. And the experimental verification result is also presented.

II. ELECTRO-MECHANICAL PARAMETER MODELING

When investigating the performance of the electric motor, the lumped parameter-based approach is the cost-efficient way. The purpose of this study is not only for seeing electric performance but also to consider mechanical characteristics. Therefore, this section introduces the electro-mechanical parameter calculation. The subject of this study was set as an electric motor for electric power steering (EPS) system. And the target of CFSM of this study is depicted in Figure 1, and the specification is organized in Table 1.

TABLE 1. Specification of concentrated flux synchronous motor for electric power steering system.

Items	Value	Unit
Pole / Slot number	14 / 18	-
Rated output power	400	W
Rated torque	3.8	Nm
Rated speed	1000	rpm
Nominal DC voltage	12	V
Rated current	60	A_{rms}

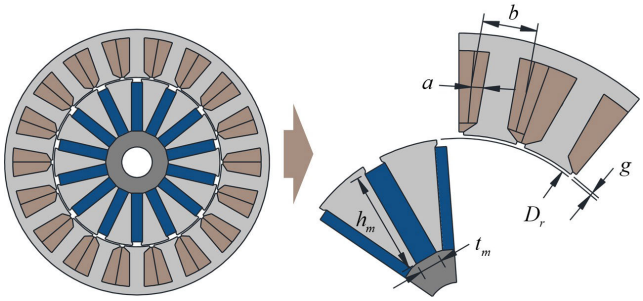

FIGURE 1. Geometry of target concentrated flux synchronous motor.

A. BACK ELECTROMOTIVE FORCE

The back EMF is proportional to the amount of the linkage flux and the rotational speed. To acquire the amount of the linkage flux, the air-gap magnetic flux density needs to be calculated. The air-gap magnetic flux density can be derived from Gauss's law and Ampere's circuital law. From Gauss's law, the relationship between the amount of the permanent magnet and the amount of the air-gap magnetic flux was obtained as equations (1) to (3) [25].

$$\int_V \nabla \cdot \vec{B} dv = \oint_S \vec{B} \cdot d\vec{S} = \Phi_m - \Phi_a = 0 \tag{1}$$

$$\Phi_m = \Phi_a \tag{2}$$

$$B_m h_m l_{stk} = B_a \frac{\pi D_r}{4p} l_{stk} \tag{3}$$

Here, Φ_m, Φ_a, B_m, B_a are magnetic flux and magnetic flux density of permanent magnet and air-gap, respectively, and h_m is height of the permanent magnet, l_{stk} is stack length of the motor, D_r is diameter of the rotor, and p is the number of the pole pairs. In this derivation, the permeability of the magnetic cores was assumed as infinite and the air gap flux distribution was assumed as a square wave.

Then, the according to the relationships of magnetic flux density and magnetic field intensity, equations (4) and (5) can be formulated. In addition, to compensate the nonlinearity and leakage flux, equation (6) was adopted. Here, B_r is the residual induction of permanent magnet, B_{r_cor} is corrected residual induction of permanent magnet, Φ_{leak} is leakage flux derived from FEA, H_m and H_a are magnetic flux intensity of permanent magnet and air-gap, μ_{rec} is recoil permeability of permanent magnet and μ_0 is permeability of air.

$$B_m = B_{r\_cor} + \mu_{rec}\mu_0 H_m \tag{4}$$

$$B_a = \mu_0 H_a \tag{5}$$

$$B_{r\_cor} = B_r - \frac{\Phi_{leak}}{h_m l_{stk}} \tag{6}$$

For the next, applying Ampere's circuital law for the flux path, equation (7) can be derived. And from equations (4) and (5), equation (7) can be transformed into equation (8), and equation (9) can be formulated. Here, t_m is the thickness of the permanent magnet, and g is the length of the air-gap.

$$\oint \vec{H} \cdot d\vec{l} = H_m t_m + H_a 2g = 0 \tag{7}$$

$$\frac{B_m - B_{r\_cor}}{\mu_{rec}\mu_0} t_m + \frac{B_a}{\mu_0} 2g = 0 \tag{8}$$

$$B_a = \frac{B_{r\_cor}}{\frac{\pi D_r}{4ph_m} + \frac{2\mu_{rec} g}{t_m}} \tag{9}$$

Finally, the armature linkage flux Ψ_a can be expressed as equation (10) considering the winding condition where the k_w is the winding factor, N is the number of armature series turns per phase. In addition, four over pi indicates the fundamental component of the square wave. Consequently, the back EMF is formulated as equation (11), where the ω_e is the electrical angular rotational speed.

$$\Psi_a = \frac{4}{\pi}\frac{k_w N}{2}\frac{D_r l_{stk}}{p} B_a \tag{10}$$

$$E_a = \omega_e \Psi_a \tag{11}$$

B. RESISTANCE

The resistance of armature winding can be calculated based on the actual structure of winding. The resistance is depending on the length of the copper wire and the cross-sectional area. To assume the structure of the winding, the stator geometry was treated in Figure 2.

Here, a denotes the height of the end turn coil, b denotes the width of the end turn coil. Therefore, the phase resistance R_a can be expressed as equation (12), where the l_c, and A_c are the length and cross-sectional area of the armature winding coil, respectively, and σ is electric conductivity of the copper.

$$R_a = \frac{l_c}{\sigma A_c} = \frac{(4a + 2b + 2l_{stk})N}{\sigma A_c} \tag{12}$$

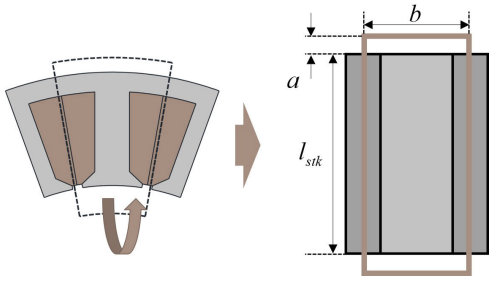

FIGURE 2. Geometric assumption of armature winding for resistance calculation.

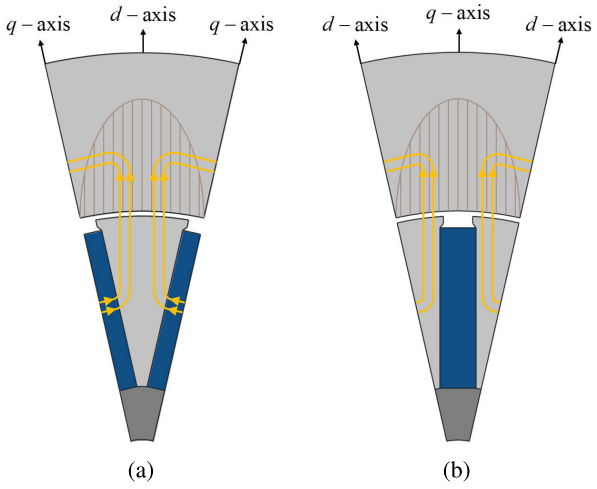

FIGURE 3. Flux path assumption for applied (a) $d-$axis current, (b) $q-$axis current.

C. INDUCTANCE

The main inductance was derived as $d-$ and $q-$axis inductance. This allows the electrical performance can be estimated utilizing the $d-q$ equivalent circuit later. For this calculation, the flux path assumption method was adopted [26]. The assumed flux paths are shown in Figure 3. Figure 3 of (a) shows the flux path for $d-$axis inductance calculation, and (b) shows the flux path for $q-$axis inductance calculation. According to each flux path, each inductance was calculated considering the reluctance and linkage flux. As a result, the $d-$ and $q-$ axis inductance can be expressed as equations (13) and (14). For this derivation, the permeability of the magnetic core was assumed as infinity.

$$L_d = \frac{3}{\pi}\frac{\mu_0 D_r l_{stk}}{g}\left(\frac{k_w N}{p}\right)^2 \left(1 - \frac{4/\pi}{\pi/2 + 4p\frac{g\mu_{rec}}{t_m}\frac{h_m}{D_r}}\right) \tag{13}$$

$$L_q = \frac{3}{\pi}\frac{\mu_0 D_r l_{stk}}{g}\left(\frac{k_w N}{p}\right)^2 \tag{14}$$

Moreover, leakage flux equations were adopted to compensate for the accuracy of the equation-based estimation [32]. They consisted of the harmonic inductance, slot leakage inductance, and shoe leakage inductance as equation (15).

$$L_{leak} = L_{har} + L_{slot} + L_{shoe} \tag{15}$$

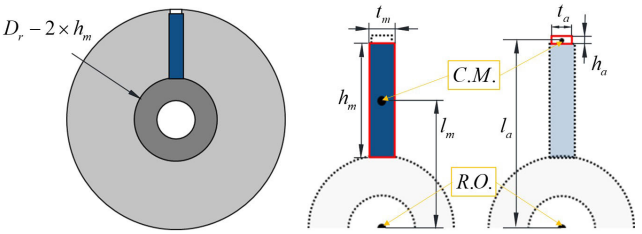

FIGURE 4. Description of rotor structure for moment of inertia calculation.

D. MOMENT OF INERTIA

The mass moment of inertia of the rotor is an essential parameter for predicting rotational dynamics. The rotor consists of core, shaft, and PM. The overall moment of inertia of the rotor was calculated as shown in equation (16). Here, J_r, J_c, J_{sh}, J_m are the mass moment of inertia of the rotor, core, shaft, PM, and p is the pole pair number.

$$J_r = J_c + J_{sh} + 2p \times J_m \tag{16}$$

For this derivation, the structure of the rotor was simplified as shown in Figure 4. The mass moment of inertia of the core, J_c was organized as equation (17), where the ρ_c is the density of the core, D_o is the outer diameter of the rotor, l_m is the distance between the mass center of PM and origin, h_a and t_a is the height and thickness of the air region, and l_a is the distance between the mass center of air region and origin. The mass moment of inertia of two squares, air region, and PM region was derived from the parallel axis theorem ($J_{m,c}, J_{a,c}$, and J_m) [27].

The mass moment of inertia of the shaft and PM are described as equations (18) and (19), where the ρ_{sh} is the density of the shaft, D_i is the inner diameter of the rotor and ρ_m is the density of the PM.

$$\begin{aligned} J_c &= J_{D_o,c} - J_{sh,c} - 2p \times J_{m,c} - 2p \times J_{a,c} \\ &\begin{cases} J_{D_o,c} = \dfrac{\pi}{32}\rho_c {D_o}^4 l_{stk} \\ J_{sh,c} = \dfrac{\pi}{32}\rho_c \left(D_o - 2\times h_m\right)^4 l_{stk} \\ J_{m,c} = \rho_c h_m t_m l_{stk}\left(l_m^2 + \dfrac{h_m^2 + t_m^2}{12}\right) \\ J_{a,c} = \rho_c h_a t_a l_{stk}\left(l_a^2 + \dfrac{h_a^2 + t_a^2}{12}\right) \end{cases} \end{aligned} \tag{17}$$

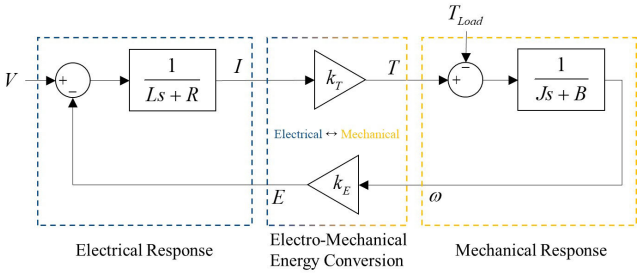

FIGURE 5. Block diagram of electric motor describing electro-mechanical response.

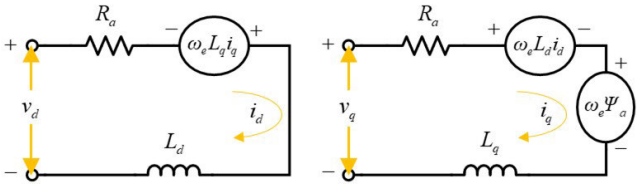

FIGURE 6. Simplified $d-q$ axis equivalent circuit of electric motor.

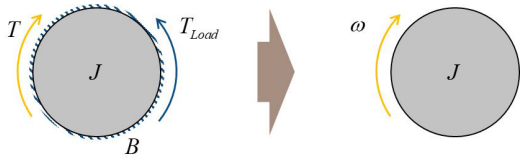

FIGURE 7. Simple rotational dynamics relationship.

$$J_{sh} = \frac{\pi}{32}\rho_{sh}\left\{\left(D_o - 2\times h_m\right)^4 - D_i^4\right\} l_{stk} \tag{18}$$

$$J_m = \rho_m h_m t_m l_{stk}\left(l_m^2 + \frac{h_m^2 + t_m^2}{12}\right) \tag{19}$$

III. ELECTRO-MECHANICAL RESPONSE MODELING

This section introduces the electro-mechanical response modeling, based on the electrical and mechanical parameters, modeled from Section II. Firstly, the electrical response is modeled through the $d-q$ axis equivalent circuit. Then, the mechanical response is modeled by the rotational dynamics equation. Finally, they were combined according to the principle of electro-mechanical energy conversion. Consequently, the equivalent transfer function of the CFSM is derived and the electro-mechanical responses are modeled. The block diagram shown in Figure 5, explains the overall relationship treated in this section.

A. ELECTRICAL RESPONSE

As mentioned in Part C of Section II, $d-q$ axis was adopted. This is not only because the equation is simple, but also clear parameter calculation process. In the same manner, the $d-q$ axis equivalent circuit as shown in Figure 6, was adopted to consider the relationship between the voltage and current [28]. It allows the investigation of the time-varying

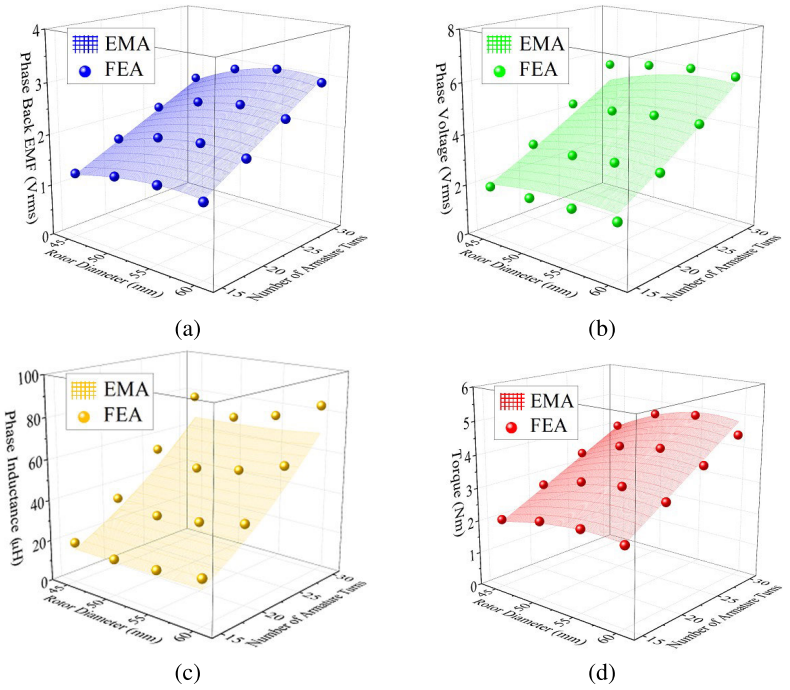

FIGURE 8. Calculation results of electrical parameters from EMA model and FEA (a) phase back EMF, (b) phase voltage, (c) phase inductance, and (d) torque.

three-phase equation to be convenient. As shown in Figure 6, this equivalent circuit can simplify the three-phase equation to a two-axis static equation. Especially, the voltage equation for steady-state can be organized as equation (20). Here, v_d and v_q are the $d-$ and $q-$ axis voltage, i_d and i_q are the $d-$ and $q-$ axis armature current.

$$\begin{aligned} v_d &= R_a i_d - \omega_e L_q i_q \\ v_q &= R_a i_q + \omega_e L_d i_d + \omega_e \Psi_a \end{aligned} \tag{20}$$

In addition, the output torque of the electric motor can be expressed as equation (21), when the $i_d = 0$ control situation.

$$T = p\Psi_a i_q \tag{21}$$

B. MECHANICAL RESPONSE

The mechanical response was modeled with a simple rotational dynamics relationship as shown in Figure 7 and equation (22). It describes the situation when applied the torque T for the rotor which has the moment of inertia J. Here, T_{Load} is load torque, B is the friction coefficient, ω, and α are angular rotational speed and angular rotational acceleration, respectively.

$$\begin{aligned} T - T_{Load} &= J\alpha + B\omega \\ &= J\frac{d\omega}{dt} + B\omega \end{aligned} \tag{22}$$

In addition, the operating condition of this motor is that the rotational speed of the rotor is not very high, and the surrounding area of the rotor consists of only air, and it is supported by the bearing. Therefore, the friction of the bearing is dominant for this case, and the friction coefficient B was used as 0.0015, which is from the bearing manufacturer [29].

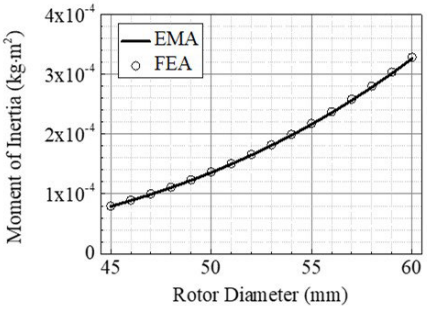

FIGURE 9. Calculation result of moment of inertia from EMA model and FEA.

C. ELECTRO-MECHANICAL RESPONSE

As shown in Figure 5, the electro-mechanical energy principle can combine the electrical response and mechanical response, and this can result in the overall electric motor system response modeling. The electrical current generates the mechanical torque, and the mechanical rotation generates the electrical back EMF. These can be expressed as equations (23) and (24), where the k_T indicates the torque constant, and k_E indicates the back EMF constant.

$$T = k_T I \tag{23}$$

$$E = k_E \omega \tag{24}$$

To apply this block diagram in electro-mechanical response modeling, the relationships as shown in equations

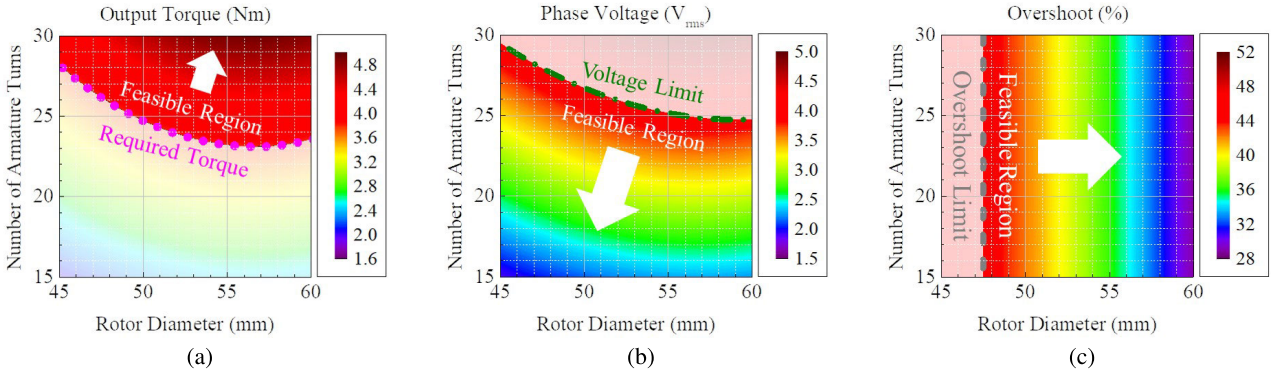

FIGURE 10. Determination of feasible design region based on EMA model.

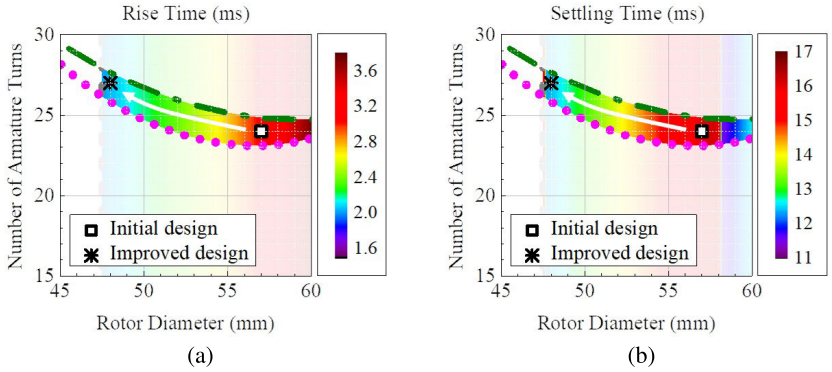

FIGURE 11. Speed response improvement design based on EMA model.

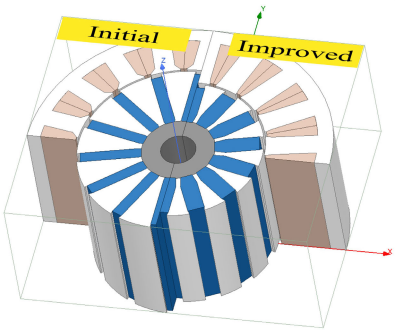

FIGURE 12. Comparison of the initial model and improved model.

from (25) to (27) were adopted [30]. And the equation of the block diagram can be organized as equations (28) and (29).

$$I = \sqrt{i_q^2 + i_d^2} \tag{25}$$

$$E = \omega_e \Psi_a \tag{26}$$

$$L = \frac{L_d + L_q + 2L_{leak}}{3} \tag{27}$$

$$V = RI + L\frac{dI}{dt} + E = RI + L\frac{dI}{dt} + k_E\omega \tag{28}$$

$$B\omega + J\frac{d\omega}{dt} + T_{Load} = T = k_T I \tag{29}$$

Then, applying the Laplace transform to equations (28) and (29), equations (30) and (31) were derived. Consequently, the equation of the closed-loop transfer function of CFSM was derived as equation (32).

$$V(s) = (R + sL)\, I(s) + k_E\omega(s) \tag{30}$$

$$T(s) = k_T I(s) = (B + sJ)\,\omega(s) + k_E\omega(s) \tag{31}$$

$$\frac{\omega(s)}{V(s)} = \frac{\frac{k_E k_T}{LJ}}{s^2 + \left(\frac{R}{L} + \frac{B}{J}\right)s + \left(\frac{RB + k_E k_T}{LJ}\right)} \tag{32}$$

From equation (32), the speed response according to voltage input was examined. Considering the characteristics of the second-order system, the natural frequency ω_n and damping ratio ζ were derived as equations (33) and (34) [31].

$$\omega_n = \sqrt{\frac{RB + k_E K_T}{LJ}} \tag{33}$$

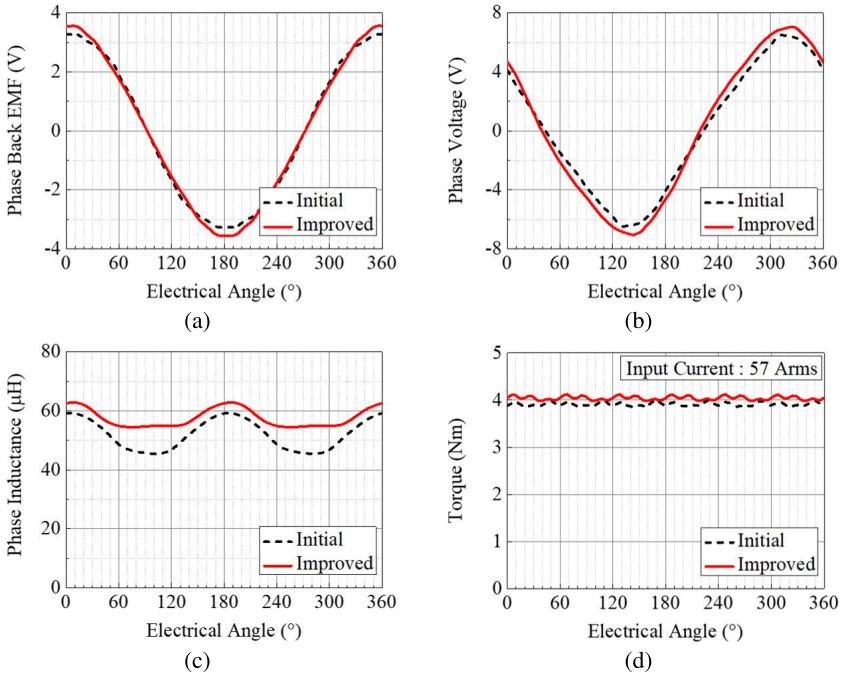

FIGURE 13. Comparison of design results based on FEA (a) phase back EMF, (b) phase voltage, (c) phase inductance, and (d) torque.

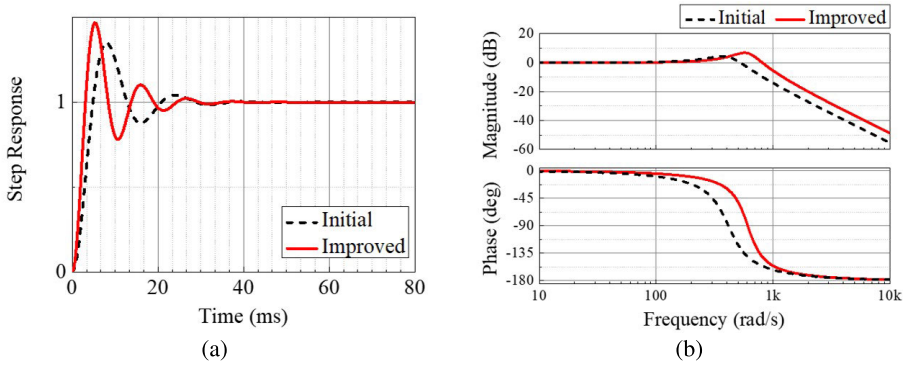

FIGURE 14. Comparison of (a) step response, and (b) bode plot for initial model and improved model.

$$\zeta = \frac{\frac{R}{L} + \frac{B}{J}}{2\sqrt{\frac{RB + k_E K_T}{LJ}}} \tag{34}$$

IV. RESULTS

A. PARAMETER MODELING RESULT

This section shows the comparison of the main parameters—phase back EMF, phase voltage, phase inductance, torque, and moment of inertia—to investigate the parameter modeling results. The parameter maps for this comparison were first generated for the entire design region using the EMA model. The FEA was then performed for several points that could cover the entire design range. These two outcomes were then compared.

The electrical parameter comparison results are shown in Figure 8. Overall, the EMA model accurately predicted the trend and value of the electrical parameters. Especially, the phase back EMF from the no-load condition was completely calculated without error. However, there were minor errors in phase voltage, phase inductance, and torque for the higher number of armature turns region. This is owing to the analytical approach's limitations, which could not reflect the non-linearity of the magnetic core.

Moreover, Figure 9 displays the calculation results of the moment of inertia. The moment of inertia from the EMA model follows the FEA result perfectly. This precision is due to the absence of non-linearity issues in the moment of inertia calculation.

B. EMA MODEL-BASED DESIGN RESULT

The usability of the developed EMA model was validated in Section IV. A. Therefore, this section introduces the speed response improvement design of the electric motor based on the proposed EMA model.

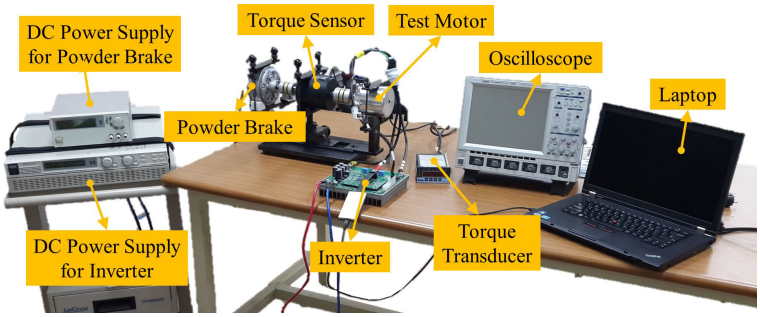

FIGURE 15. Test bench setup for experimental validation.

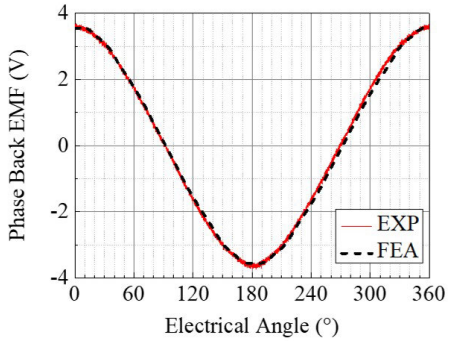

FIGURE 16. Comparison of phase back EMF from no-load test and FEA.

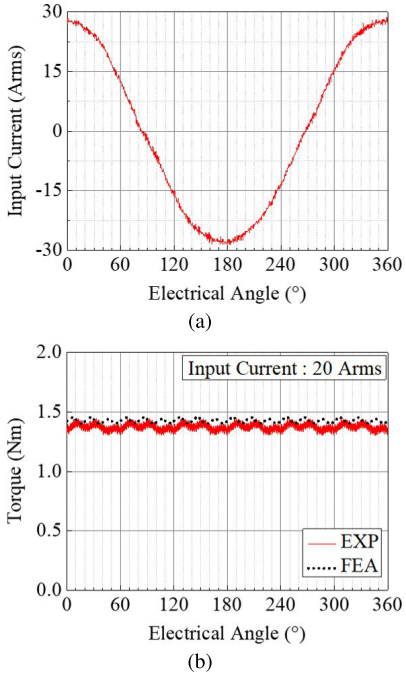

FIGURE 17. Load test results (a) input current, and (b) torque.

First, the feasible design region was determined as shown in Figure 10. The torque limit was determined based on the required torque from the target specification, as depicted in Figure 10 (a). In addition, the phase voltage limit was assigned based on the DC link voltage, as illustrated in Figure 10 (b). Furthermore, as shown in Figure 10 (c), the percentage of overshoot is limited.

TABLE 2. Design result.

Items	Value (EMA / FEA)	
	Initial	Improved
Phase Back EMF (Vrms)	2.42 / 2.39	2.43 / 2.46
Phase Voltage (Vrms)	4.37 / 4.26	4.62 / 4.79
Phase Inductance (μH)	43.74 / 49.98	53.97 / 57.57
Torque (Nm)	3.95 / 3.91	3.97 / 4.04
Moment of Inertia (kg· cm^2)	2.56 / 2.58	1.11 / 1.11
Rise Time (ms)	3.09 / 3.25	2.05 / 2.06
Settling Time (ms)	16.04 / 17.75	12.47 / 16.62

The speed response improvement design was then carried out within the determined feasible design region, as shown in Figure 11. This procedure took into account not only the rise time but also the settling time. Within the same outer size, the rotor diameter was decreased from 57 mm to 48 mm, and the number of armature turns was increased from 24 turns to 27 turns. The comparison between the initial model and the improved model is shown in Figure 12.

The design results were organized in Table 2. The main parameters of the initial and improved models are compared. In addition, a comparison of calculation results from the EMA model and FEA is provided. The following parameters are compared: phase back EMF, phase voltage, phase inductance, torque, and moment of inertia. Furthermore, the rise and settling times of the open loop step response are compared. In addition, the FEA results of electrical parameters are compared in Figure 13. Moreover, the unit-step response and bode plot are illustrated in Figure 14. The faster response can be confirmed according to Figure 14 (a). In addition, the wider bandwidth can be confirmed according to Figure 14 (b). A wider bandwidth provides a greater response to higher input frequencies. Subsequently, the EPS system, it may be stated, can respond more quickly to critical circumstances.

C. EXPERIMENTAL VALIDATION RESULT

A prototype of the improved model was built to test the effectiveness of the suggested design process. The test bench was configured as shown in Figure 15. This configuration displays the load and speed response tests. For the case of conducting the no-load test, the powder brake of Figure 15 was replaced with a DC servo motor.

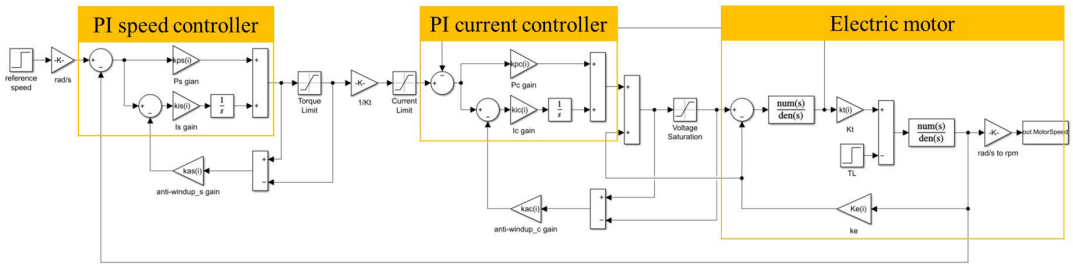

FIGURE 18. Simulink model for speed and current controlled speed response simulation.

The no-load phase back EMF was first measured. After disconnecting the test motor and inverter, the test motor and Y-connected resistors were connected. And the powder brake was replaced with a DC servo motor that was powered by a DC power supply. Then, the input voltage of the servo motor was controlled to rotate the test motor at 1000 rpm. Finally, the no-load phase back EMF was measured and the result is depicted in Figure 16.

Next, the load test was performed. The load test was performed within 20 Arms input current to ensure stable conditions. When the input current is 20 Arms, the output torque is less than 1.5 Nm, which is 50% of the powder brake's maximum capacity. The measured input current and output torque are shown in Figure 17. At this time, due to the resolution of the torque sensor, the torque was measured at 100 rpm.

Finally, the speed response test was carried out. The speed and current controlled speed response were examined to assess their practical effectiveness. Accordingly, simulation was also performed for the case of speed and current controlled test situation. As shown in Figure 18, the simulation was carried out using MATLAB Simulink, which includes a PI speed and current controller, an electric motor model, anti-windup gain, and limits (torque, current, voltage). The limits of torque, current, and voltage were set considering the actual test conditions. The parameters of the electric motor reflected the FEA result of Table 2. In addition, PI speed and current controller gains and their anti-windup gains are calculated according to equations from (35) to (40) [30]. Here, ω_{cc} and ω_{cs} are the cut-off frequency of current and speed controller, k_{Pc}, k_{Ic}, and k_{AWc} are P gain, I gain, and anti-windup gain of PI current controller, k_{Ps}, k_{Is}, and k_{AWs} are P gain, I gain, and anti-windup gain of PI speed controller.

$$k_{Pc} = \omega_{cc} L \tag{35}$$

$$k_{Ic} = \omega_{cc} R \tag{36}$$

$$k_{AWc} = \frac{1}{k_{Pc}} \tag{37}$$

$$k_{Ps} = \frac{\sqrt{\omega_{cs}^2 J^2 + B^2}}{k_T} \tag{38}$$

$$k_{Is} = \frac{\omega_{cs}\sqrt{\omega_{cs}^2 J^2 + B^2}}{5k_T} \tag{39}$$

$$k_{AWs} = \frac{1}{k_{Ps}} \tag{40}$$

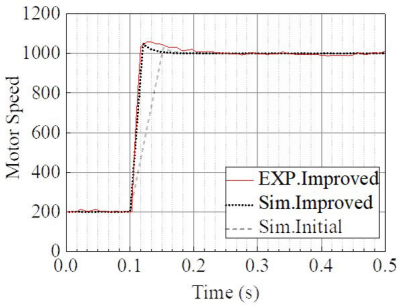

FIGURE 19. Comparison of speed response test result from simulation and experiment.

The following conditions were used in the test and simulation: 1)1.4 Nm torque is applied, and 2) the test motor is steadily rotated at 200 rpm 3) ideal PI controller gains considering pole-zero cancellation are applied. This condition allowed the test to rule out the possibility of additional mechanical friction from the starting situation. Figure 19 compares the simulation and experiment speed response test results. In addition, the simulation result of the initial model was shown to demonstrate the effect of the suggested design process.

V. CONCLUSION

The speed response enhancement design of rare-earth-free CFSM was obtained by this study. The EMA model, which could estimate not only electrical performance but also the mechanical response, was initially developed to establish the design direction. This EMA model was validated by comparing the parameter calculation results from the EMA model and FEA. Overall, there were no discrepancies between the results from the EMA model and FEA. There were minor errors for the highest number of armature turns, where the nonlinearity of the magnetic core had a significant impact. This is the limit of this study, and if the nonlinearity of the magnetic core is considered in future work, this study may be applied broadly in CFSM design and optimization. Furthermore, the improved model was fabricated as a prototype, and experiments were carried out. The findings of the back EMF and load torque tests confirmed the electrical performance prediction. And the electro-mechanical speed response estimation was validated by the speed response test result. In conclusion, the suggested EMA can consider the electro-mechanical response and can be utilized in the speed response improvement design process of CFSM.

ABBREVIATIONS

- ADAS Advanced Driver Assistant System
- CFSM Concentrated Flux Synchronous Motor
- DC : Direct Current
- EMA: Electro-Mechanical Analytic
- EMF : Electro-Motive Force
- EPS : Electric Power Steering
- EV : Electric Vehicle
- FEA : Finite Element Analysis
- HEV : Hybrid Electric Vehicle
- PM : Permanent Magnet

LIST OF SYMBOLS

- a : Height of the end turn coil of armature winding, m
- b : Width of the end turn coil of armature winding, m
- g : Length of the air-gap, m
- h_a : Height of the air region, m
- h_m : Height of the PM, m
- i_d : d-axis current, A
- i_q : q-axis current, A
- k_E : Back EMF coefficient, V·sec/rad
- k_T : Torque coefficient, Nm/A
- k_{AWc} : Anti-windup gain of PI current controller, -
- k_{AWs} : Anti-windup gain of PI speed controller, -
- k_{Ic} : I gain of PI current controller, -
- k_{Is} : I gain of PI speed controller, -
- k_{Pc} : P gain of PI current controller, -
- k_{Ps} : P gain of PI speed controller, -
- k_w : Winding factor, -
- l_a : Distance between the mass center of air region and origin, m
- l_c : Length of the armature winding coil, m
- l_m : Distance between the mass center of PM and origin, m
- l_{stk} : Stack length of the motor, m
- p : The number of the pole pairs, -
- t_a : Thickness of the air region, m
- t_m : Thickness of PM, m
- v_d : d-axis voltage, V
- v_q : q-axis voltage, V
- A_c : Cross-sectional area of the armature winding coil, m^2
- B : Friction coefficient, Nm·sec
- B : Magnetic flux density, T
- B_a : Magnetic flux density of air-gap, T
- B_m : Magnetic flux density of PM, T
- B_r : Residual induction of PM, T
- B_{r_cor}: Corrected residual induction of PM, T
- D_i : Inner diameter of the rotor, m
- D_o : Outer diameter of the rotor, m
- D_r : Diameter of the rotor, m
- E : Back EMF, V
- H_a : Magnetic flux intensity of air-gap, A/m
- H_m : Magnetic flux intensity of PM, A/m
- I : Input current, A
- J : Mass moment of inertia, kg·m^2
- $J_{a,c}$: Mass moment of inertia of core for air region, kg·m^2
- J_c : Mass moment of inertia of core, kg·m^2
- $J_{Do,c}$: Mass moment of inertia of core for whole rotor region, kg·m^2
- J_m : Mass moment of inertia of PM, kg·m^2
- $J_{m,c}$: Mass moment of inertia of core for PM region, kg·m^2
- J_r : Mass moment of inertia of rotor, kg·m^2
- J_{sh} : Mass moment of inertia of shaft, kg·m^2
- $J_{sh,c}$: Mass moment of inertia of core for shaft region, kg·m^2
- L : Inductance, H
- L_d : d-axis inductance, H
- L_q : q-axis inductance, H
- L_{har} : Leakage inductance of harmonic components, H
- L_{leak} : Leakage inductance, H
- L_{shoe} : Leakage inductance of shoe, H
- L_{slot} : Leakage inductance of slot, H
- N : The number of armature winding series turns per phase, -
- R : Resistance, Ω
- R_a : Phase resistance of armature winding, Ω
- T : Torque, Nm
- T_{Load} : Load torque, Nm
- α : Angular acceleration, rad/s^3
- ζ : Damping ratio, -
- μ_0 : Permeability of air, H/m
- μ_{rec} : Recoil permeability of PM, -
- ρ_c : Density of the core, kg/m^3
- ρ_m : Density of the PM, kg/m^3
- ρ_{sh} : Density of the shaft, kg/m^3
- σ : Electric conductivity of the armature winding coil, S/m
- ω : Mechanical angular rotational speed, rad/s
- ω_{cc} : Cut-off frequency of PI current controller, rad/s
- ω_{cs} : Cut-off frequency of PI speed controller, rad/s
- ω_e : Electrical angular rotational speed, rad/s
- ω_n : Natural frequency, rad/s
- Φ_a : Magnetic flux of air-gap, Wb
- Φ_{leak} : Leakage magnetic flux, Wb
- Φ_m : Magnetic flux of permanent magnet, Wb
- Ψ_a : Linkage flux of armature winding, Wb

ACKNOWLEDGMENT

This study was supported by research fund from Honam University, 2021

REFERENCES

[1] M. E. Riddle, E. Tatara, C. Olson, B. J. Smith, A. B. Irion, B. Harker, D. Pineault, E. Alonso, and D. J. Grazianon, "Agent-based modeling of supply disruptions in the global rare earths market," *Resour. Conserv. Recycl.*, vol. 164, Jan. 2021, Art. no. 105193, doi: 10.1016/j.resconrec.2020.105193.

[2] K. Roelich, D. A. Dawson, P. Purnell, C. Knoeri, R. Revell, J. Busch, and J. K. Steinberger, "Assessing the dynamic material criticality of infrastructure transitions: A case of low carbon electricity," *Appl. Energy*, vol. 123, pp. 378–386, Jun. 2014, doi: 10.1016/j.apenergy.2014.01.052.

[3] K. Frost, I. Sousa, J. Larson, H. Jin, and I. Hua, "Environmental impacts of a circular recovery process for hard disk drive rare earth magnets," *Resour. Conserv. Recycl.*, vol. 173, Oct. 2021, Art. no. 105694, doi: 10.1016/j.resconrec.2021.105694.

[4] B. Ballinger, M. Stringer, D. R. Schmeda-Lopez, B. Kefford, B. Parkinson, C. Greig, and S. Smart, "The vulnerability of electric vehicle deployment to critical mineral supply," *Appl. Energy*, vol. 255, Dec. 2019, Art. no. 113844, doi: 10.1016/j.apenergy.2019.113844.

[5] J. D. Widmer, R. Matrin, and M. Kimiabeigi, "Electric vehicle traction motors without rare earth magnets," *Sustain. Mater. Technol.*, vol. 3, pp. 7–13, Apr. 2015, doi: 10.1016/j.susmat.2015.02.001.

[6] B. Poudel, E. Amiri, P. Rastgoufard, and B. Mirafzal, "Toward less rare-earth permanent magnet in electric machines: A review," *IEEE Trans. Magn.*, vol. 57, no. 9, pp. 1–19, Sep. 2021, doi: 10.1109/TMAG.2021.3095615.

[7] E. Sayed, S. M. Castano, J. W. Jiang, J. Liang, G. Pietrini, M. H. Bakr, A. Emadi, and B. Bilgin, "Design of multilayer concentric ferrite-magnet machines for a traction application," *IEEE Trans. Transport. Electrific.*, vol. 7, no. 3, pp. 1548–1560, Sep. 2021, doi: 10.1109/TTE.2020.3042623.

[8] N.-F. Jurca, R. A. Inte, D.-C. Popa, B. Varaticeanu, P. Minciunescu, and C. Martis, "Electromagnetic and mechanical analysis of a modular outer rotor synchronous reluctance machine for light propulsion vehicles," *IEEE Trans. Transport. Electrific.*, vol. 7, no. 4, pp. 2798–2811, Dec. 2021, doi: 10.1109/TTE.2021.3067135.

[9] J.-R. Riba, C. López-Torres, L. Romeral, and A. Garcia, "Rare-earth-free propulsion motors for electric vehicles: A technology review," *Renew. Sustain. Energy Rev.*, vol. 57, pp. 367–379, May 2016, doi: 10.1016/j.rser.2015.12.121.

[10] TDK. *Application Guide—Automotive*. Accessed: Feb. 15, 2022. [Online]. Available: https://product.tdk.com/en/applicationguide/magnet/ap_automotive.html

[11] A. Bollero and E. M. Palmero, "Recent advances in hard ferrite magnets," in *Modern Permanent Magnets*, J. Croat and J. Ormerod, Eds. Cambridge, U.K.: Woodhead, 2022, pp. 65–112, doi: 10.1016/B978-0-323-88658-1.00013-3.

[12] D.-M. Kim, K.-S. Cha, M.-S. Lim, and J.-P. Hong, "Rare-earth-free electric motor design for EV traction comparing overall vehicle efficiency considering driving cycle," in *Proc. IEEE 84th Veh. Technol. Conf. (VTC-Fall)*, Montreal, QC, Canada, Sep. 2016, pp. 1–5, doi: 10.1109/VTCFall.2016.7881188.

[13] S. G. Lee, J. Bae, and W.-H. Kim, "Design process of spoke-type permanent magnet synchronous motor considering magnetization performance," *IEEE Trans. Appl. Supercond.*, vol. 30, no. 4, pp. 1–6, Jun. 2020, doi: 10.1109/TASC.2020.2986968.

[14] M.-R. Park, J.-W. Jung, D.-Y. Kim, J.-P. Hong, and M.-S. Lim, "Design of high torque density multi-core concentrated flux-type synchronous motors considering vibration characteristics," *IEEE Trans. Ind. Appl.*, vol. 55, no. 2, pp. 1351–1359, Mar. 2019, doi: 10.1109/TIA.2018.2876329.

[15] C. Seok, H. Choi, and J. Seo, "Design and analysis of a novel spoke-type motor to reduce the use of rare-earth magnet materials," *IET Electric Power Appl.*, vol. 15, no. 11, pp. 1479–1487, Nov. 2021, doi: 10.1049/elp2.12109.

[16] Y.-R. Lee, Y.-C. Kwon, and S.-K. Sul, "Realization of signal-injection sensorless control of SMPMSM with saturation-induced saliency by modification of current trajectory," *IEEE Trans. Power Electron.*, vol. 37, no. 11, pp. 13277–13287, Nov. 2022, doi: 10.1109/TPEL.2022.3186609.

[17] M.-S. Lim, S.-H. Chai, and J.-P. Hong, "Design of saliency-based sensorless-controlled IPMSM with concentrated winding for EV traction," *IEEE Trans. Magn.*, vol. 52, no. 3, pp. 1–4, Mar. 2016, doi: 10.1109/TMAG.2015.2474123.

[18] D.-K. Son, D.-K. Kang, D.-I. Son, S.-H. Kwon, and G.-H. Lee, "Hybrid mode control of an asymmetric dual three-phase synchronous motor under single-phase open fault," *IEEE Access*, vol. 10, pp. 53250–53264, 2022, doi: 10.1109/ACCESS.2022.3176019.

[19] B.-K. Song, J.-W. Chin, D.-M. Kim, K.-Y. Hwang, and M.-S. Lim, "Temperature estimation using lumped-parameter thermal network with piecewise stator-housing modules for fault-tolerant brake systems in highly automated driving vehicles," *IEEE Trans. Intell. Transp. Syst.*, vol. 22, no. 9, pp. 5819–5832, Sep. 2021, doi: 10.1109/TITS.2021.3091621.

[20] M.-S. Lim, J.-M. Kim, Y.-S. Hwang, and J.-P. Hong, "Design of an ultra-high-speed permanent-magnet motor for an electric turbocharger considering speed response characteristics," *IEEE/ASME Trans. Mechatronics*, vol. 22, no. 2, pp. 774–784, Apr. 2017, doi: 10.1109/TMECH.2016.2634160.

[21] A. Varshney, D. Gupta, and B. Dwivedi, "Speed response of brushless DC motor using fuzzy PID controller under varying load condition," *J. Electr. Syst. Inf. Technol.*, vol. 4, no. 2, pp. 310–321, Sep. 2017, doi: 10.1016/j.jesit.2016.12.014.

[22] J. Gao, C. Li, L. Dai, S. Huang, and W. Xu, "A practical analytical expression and estimation for average torque of high saturation permanent magnet synchronous motor for special vehicles," *IEEE Trans. Veh. Technol.*, vol. 72, no. 1, pp. 357–366, Jan. 2023, doi: 10.1109/TVT.2022.3202353.

[23] B. Dianati, S. Kahourzade, and A. Mahmoudi, "Optimization of axial-flux induction motors for the application of electric vehicles considering driving cycles," *IEEE Trans. Energy Convers.*, vol. 35, no. 3, pp. 1522–1533, Sep. 2020, doi: 10.1109/TEC.2020.2976625.

[24] P. Liang, F. Chai, Y. Yu, and L. Chen, "Analytical model of a spoke-type permanent magnet synchronous in-wheel motor with trapezoid magnet accounting for tooth saturation," *IEEE Trans. Ind. Electron.*, vol. 66, no. 2, pp. 1162–1171, Feb. 2019, doi: 10.1109/TIE.2018.2831194.

[25] D. K. Cheng, "Static magnetic fields," in *Fundamentals of Engineering Electromagnetics*. Boston, MA, USA: Addison-Wesley, 1993.

[26] N. Bianchi and T. M. Jahns, "Design, analysis, and control of interior PM synchronous machines," in *Proc. IEEE IAS Annu. Meeting*, Seattle, DC, USA, Oct. 2004, pp. 3-8–3-24.

[27] F. P. Beer, E. R. Johnston, P. Cornwell, B. Self, and S. Sanghi, "Kinetics of particles: Energy and momentum methods," in *Vector Mechanics for Engineers: Dynamics*. New York, NY, USA: McGraw-Hill, 2019.

[28] D. Kim, J. Chin, J. Hong, and M. Lim, "Performance prediction of surface-mounted permanent magnet synchronous motor based on ring specimen test result," *IET Electric Power Appl.*, vol. 13, no. 9, pp. 1280–1286, Sep. 2019, doi: 10.1049/iet-epa.2018.5382.

[29] SKF. *Rolling Bearing Catalogue*. Accessed: Feb. 15, 2022. [Online]. Available: http://www.skf.com/binaries/pub12/Images/0901d196802809de-Rolling-bearings—17000_1-EN_tcm_12-121486.pdf

[30] S.-H. Kim, "Control of direct current motors," in *Electric Motor Control: DC, AC and BLDC Motors*. Amsterdam, The Netherlands: Elsevier, 2017.

[31] M. F. Golnaraghi and B. C. Kuo, "Time-domain analysis of control systems and frequency-domain analysis," in *Automatic Control Systems*. Hoboken, NJ, USA: Wiley, 2010.

[32] T. A. Lipo, "Main flux path calculations using magnetic circuits and use of magnetic circuits in leakage reactance calculations," in *Introduction to AC Machine Design*. Hoboken, NJ, USA: Wiley, 2017.

DONG-MIN KIM (Member, IEEE) received the Ph.D. degree in automotive engineering from Hanyang University, Seoul, South Korea, in 2021. Since 2021, he has been with Honam University, Gwangju, South Korea, where he is currently an Assistant Professor. His research interests include the design optimization of electric machines for automotive and industrial applications, modeling and optimization of hybrid electric vehicles, electric vehicles, and fuel cell electric vehicles.

MYUNG-SEOP LIM (Member, IEEE) received the bachelor's degree in mechanical engineering and the master's and Ph.D. degrees in automotive engineering from Hanyang University, Seoul, South Korea, in 2012, 2014, and 2017, respectively. From 2017 to 2018, he was a Research Engineer with Hyundai Mobis, Yongin, South Korea. In 2018, he was an Assistant Professor with Yeungnam University, Daegu, South Korea. Since 2019, he has been with Hanyang University, where he is currently an Assistant Professor. His research interests include electromagnetic field analysis and the design of electric machinery for mechatronics systems.